Fine sediment in mixed sand-silt environments impact bedform geometry by altering sediment mobility

de Lange, S.L.; Niesten, I.; van de Veen, S.H.J.; Baas, Jaco; Lammers, J.; Waldschlaeger, K.; Boelee, D.; Hoitink, A.J.F.

Water Resources Research

DOI:
10.1029/2024WR037065

Published: 01/07/2024

Peer reviewed version

Fine sediment in mixed sand-silt environments impacts bedform geometry by altering sediment mobility

S.I. de Lange[1], I. Niesten[1], S.H.J. van de Veen[1], J.H. Baas[2], J. Lammers[1], K. Waldschläger[1], D. Boelee[1], A.J.F. Hoitink[1]

[1]Wageningen University, Department of Environmental Sciences, Hydrology and Environmental Hydraulics, Wageningen, the Netherlands
[2]School of Ocean Sciences, Bangor University, Menai Bridge, United Kingdom

Key Points:

- An increased dune length due to a larger fraction of finer, non-cohesive material in a sand bed, implies an increased mobility of the sand.
- A decreased dune size due to a larger fraction of finer, weakly-cohesive silt in a sand bed, implies a decreased mobility of the sand.
- Sediment bed composition indirectly affects hydraulic roughness by altering bedform geometry.

Corresponding author: Sjoukje de Lange, `sjoukje.delange@wur.nl`

Abstract

Geometric characteristics of subaqueous bedforms, such as height, length and leeside angle, are crucial for determining hydraulic form roughness and interpreting sedimentary records. Traditionally, bedform existence and geometry predictors are primarily based on uniform, cohesionless sediments. However, mixtures of sand, silt and clay are common in deltaic, estuarine, and lowland river environments, where bedforms are ubiquitous. Therefore, we investigate the impact of fine sand and silt in sand-silt mixtures on bedform geometry, based on laboratory experiments conducted in a recirculating flume. We systematically varied the fraction of sand and silt for different discharges, and utilized an acoustic Doppler velocimeter to measure flow velocity profiles. The final bed geometry was captured using a line laser scanner. Our findings reveal that the response of bedforms to an altered fine sediment percentage is ambiguous, and likely depends on, among others, bimodality-driven bed mobility and sediment cohesiveness. When fine, non-cohesive material (fine sand or coarse silt) is mixed with the base material (medium sand), an increased dune height and length is observed, possibly caused by the hiding-exposure effect, resulting in enhanced mobility of the coarser material. However, weakly-cohesive fine silt suppresses dune height and length, possibly caused by reduced sediment mobility. Finally, in the transition from dunes to upper stage plane bed, there are indications that the bed becomes unstable and dune heights vary over time. The composition of the bed material does not significantly impact the hydraulic roughness, but mainly affects roughness via the bed morphology, especially the leeside angle.

Plain Language Summary

Underwater bedforms, such as dunes, are often found on the bed of rivers and deltas. These rhythmic undulations have specific shapes and sizes, and they affect how water flows. When the bed of the river is made up of sand, we can predict the dune height and length. However, mixtures of different-sized sediments are common in rivers, and it is unknown how this impacts the geometry of the dunes. Therefore, we did experiments in a flume, a laboratory facility to simulate a river, and we tested different sediment bed mixtures. We found that replacing part of the base material with non-cohesive fine particles leads to longer dunes, likely caused by increased mobility of the base material. However, for weakly-cohesive fine particles, the effect was the opposite, and the dunes became shorter, probably due to the limited mobility of the sediment. Finally, we observed that under high flow conditions, the bed became unstable and different dune shapes occurred. We found that the friction the water experiences is not directly impacted by the sediment bed mixtures, but is mostly affected by the shape of the bedforms.

1 Introduction

River bedforms are ubiquitous in low-land rivers, and they are known to impact the river by altering its hydraulics, ecology, and sediment balance. The geometry of river bedforms, especially dunes, impacts the fairway depth (ASCE Task Force, 2002; Best, 2005), adds to the form roughness of the river bed (Warmink et al., 2013; Venditti and Bradley, 2022), and determines suitable foraging places for fish (Greene et al., 2020). It is therefore useful to predict the geometry of bedforms without having to perform regular field measurements. In non-supply limited conditions, river dunes may scale with flow depth (Allen, 1978). However, more recent studies have reinstated the observations by Yalin (1964), van Rijn (1984), and Karim (1995), indicating a relation between bedform geometry and some measure of transport stage (Bradley and Venditti, 2019; Venditti and Bradley, 2022), where transport stage represents the ratio between flow strength and the mobility of the bed material. Dune length increases with transport stage, while dune height increases with transport stage until a maximum is reached, whereafter the height decreases and the bedforms start to wash out (Baas and Koning, 1995; Bradley and Venditti, 2019). This framework effectively predicts dune height and length, despite considerable variability, which can be up to two-orders of magnitude (Bradley and Venditti, 2017). This variability may in part be attributed to the influence of bed composition on bedform geometry.

The bed composition, i.e. the grain size distribution of the bed sediment, is one of the primary determinants for bedform presence and size. Measures of grain size appear in almost all existing phase diagrams (Southard and Boguchwal, 1990; van den Berg and Gelder, 1993; Perillo et al., 2014), with the median grain size D_{50} as general parameterization. However, this simplification poses challenges when dealing with natural sediment mixtures characterized by complex, multimodal sediment size distributions, which are common in deltaic, estuarine and coastal environments featuring sediment mixtures of mud (i.e. clay and silt) and sand (Healy et al., 2002).

Recent research has focused on understanding how cohesive clay affects bedform geometry. It has been observed that even a small percentage of cohesive clay in sand-clay mixtures can effectively suppress bed mobility, resulting in a reduced bedform height (Schindler et al., 2015; Parsons et al., 2016) and limited bedform growth (Wu et al., 2022). It is, however, unknown what the impact of non- and weakly cohesive fine materials (silts and fine sands) is on dune morphology, despite their abundance in deltaic environments.

A few studies explored the influence of silt on erodibility of the sediment bed. For instance, Bartzke et al. (2013) examined the behavior of sand (300 μm)-silt (50 μm) beds in an annular laboratory flume. They found that an increasing silt content, even at low percentages (as little as 0.18% silt), contributed to bed stabilization through a reduction in water inflow, attributed to pore-space plugging by silt. Yao et al. (2022) also reported increased stability (i.e., increased erosion threshold) with increasing silt content in their laboratory experiments, although stabilization only occurred at a silt content of >35%, when a stable silt skeleton could be formed. Opposing Bartzke et al. (2013), a change in bed stability was not observed at lower silt contents.

Additionally, Ma et al. (2017) and Ma et al. (2020) studied a silt-rich sediment bed (D_{50} = 15 - 150 μm) with low dunes in the Yellow River. Ma et al. (2020) showed that the presence of fine sediment (silt) led to a shift from a low-efficiency sediment transport regime (following the Engelund-Hansen equations (Engelund and Hansen, 1967)) to a high-efficiency regime, during which sediment transport is higher than predicted using the Engelund-Hansen equations. The high-efficiency regime prevailed for sediment beds with a medium grain size smaller than 88 μm, and, in the transitional range (88 μm < D_{50} < 153 μm), the existence of this regime depended on sorting of the material ($\sqrt{D_{84}/D_{16}}$). They argued that the shift from a low- to a high-efficiency transport regime resulted from the transition from mixed load to suspended sediment transport, caused by the presence of silt.

Yet, none of these studies discussed the potential impact of silt content on bedforms. This is an important research gap, because an increase in bed stability, as observed by Bartzke et al. (2013) and Yao et al. (2022), could theoretically reduce bedform formation and growth due to a decrease in sediment transport, whilst Ma et al. (2020)'s suspension-load dominated high-efficiency regime would also mean suppression of bedform formation and growth, but then because bedload transport gets increasingly replaced by suspended load transport, which is incapable of forming bedforms. Clearly, the effect of silt in sand-silt mixtures on the resulting bedform geometry is largely unexplored. Therefore, our research seeks to address the following question: What is the influence of the fraction non-cohesive and weakly cohesive fine sediment in sand-silt mixtures on the dynamic equilibrium bedform geometry and the resulting hydraulic roughness?

To answer this question, we conducted 51 laboratory experiments in a recirculating flume, in which the influence of fine sand and silt percentage in sand-silt mixtures on bedform geometry was studied. For three flow velocities, 17 different sediment mixtures, largely falling within the transitional range of grain sizes of Ma et al. (2020) (88 μm < D_{50} <

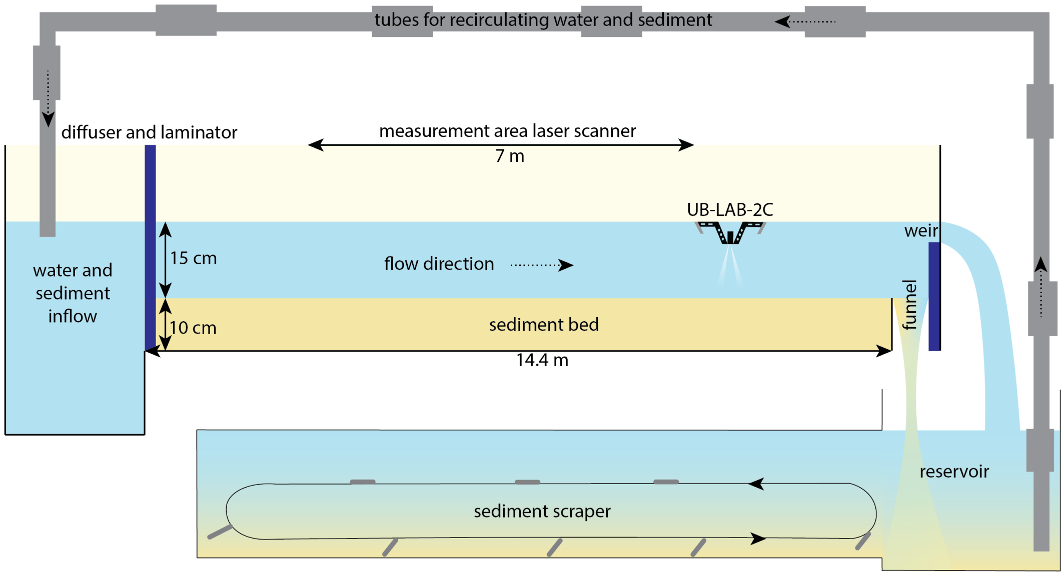

Figure 1. Schematic drawing of the experimental setup. The flume recirculates both water and sediment.

153 μm), were tested by systematically mixing various fractions of fine sand, coarse silt and fine silt with a coarser base material of medium sand. These experiments allowed us to assess how different sizes of fine sediment in a sand-silt mixture affect the transport stage and the resulting bedform geometry under different flow conditions. In the following sections, we provide a detailed description of the experimental setup, after which we discuss the different bedform geometries that resulted from the experiments. We expect that the hiding-exposure effect enhances the mobility of the coarser fraction, whereas cohesion from fine silt decreases the bed mobility, leading to deviations from the expected relationship between transport stage and dune dimensions.

2 Methods

2.1 Experimental setup

The experiments were conducted in a tilting flume with recirculation facilities for both water and sediment in the Kraijenhoff van de Leur Laboratory for Water and Sediment Dynamics of Wageningen University and Research (Figure 1 and 2). The flume has an internal width of 1.20 m, a length of 14.4 m, and a height of 0.5 m. The water level is controlled by adjusting a downstream weir. A diffuser (Figure 2a) at the upstream part ensures that the inflow is distributed over the entire width of the flume. The diffuser is followed by a stacked pile of PVC tubes that serve as a laminator, suppressing turbulence at the inflow section. At the end of the flume, a funnel was installed to channel bedload material to a lower reservoir (Figure 1), and to prevent deposition in front of the weir. A continuously running sediment scraper ensures that the sediment stays in suspension in the lower reservoir, upon being pumped back to the inflow of the flume. At the end of one experiment (35% fine sand, medium discharge) the sediment funnel was clogged and the sediment was not fully recirculated. This run was excluded from the analysis.

The flow depth in the measurement range was about 15 cm, measured from the initial flat sediment bed, and it was kept the same for all experimental runs by adjusting the weir height. The initial bed slope was set to 0.01 m m^{-1}, and kept constant for all experiments.

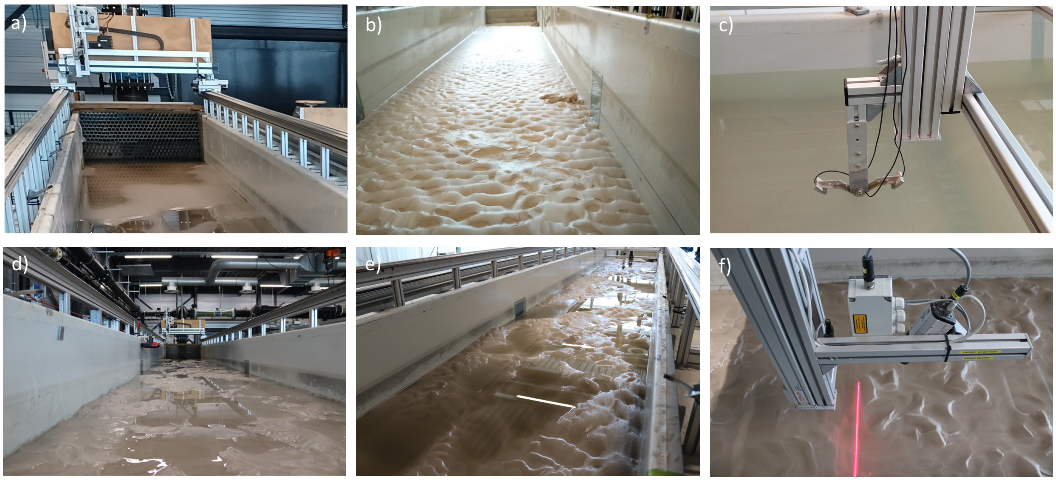

Figure 2. Pictures of the laboratory flume and the instrumentation. a) Flume with flatbed, facing upstream, including the upstream-located diffuser. b) Bed covered with ripples, facing downstream, including the downstream-located weir. c) UB-Lab 2C flow velocity profiler. d) Dune-covered bed, facing upstream. e) Dune-covered bed, facing downstream, with the UB-Lab 2C in background. f) Line laser scanner.

The duration of the experiments was long enough for the bed to adjust to near-uniform flow conditions. Experimental runs were performed for different discharges (low: 45 L s^{-1}; medium: 80 L s^{-1}; high: 100 L s^{-1}). The discharge was monitored with an electromagnetic flow meter, and regulated based on the online flow meter readings to achieve a stable flow rate in the flume The corresponding calculated width- and depth-averaged flow velocities were 0.25, 0.44 and 0.56 m s^{-1}; the corresponding depth-averaged flow velocities in the middle of the flume (measured with an UB-Lab 2C, see section 2.2) were slightly larger due to drag with the side walls (0.30, 0.45 and 0.58 m s^{-1}, respectively). The experiments were run for 12, 5 and 3 hours for the low, medium, and high discharges, respectively. To be able to compare the experiments with each other, bedforms need to be in equilibrium. Based on the ripple size predictor of Soulsby et al. (2012), the medium-sand ripples formed in the low-discharge experiments reached about 80% of their equilibrium height and length after 12 hours. Their planform at this development stage was linguoid, which agrees with the planform predicted by ripple development model of Baas (1999). Naqshband et al. (2016) studied the dune equilibrium time for medium sand (290 μm). Their equilibrium dimensions were reached after 3 hours for the experiments with a flow velocity of 0.64 m s^{-1} and after 1.5 hours for 0.80 m s^{-1}. This suggests that the dunes formed at medium and high discharges in the present experiments were close to equilibrium size.

The flow was sub-critical and turbulent during all experiments, determined by the Froude number, *Fr* (-), being smaller than 1 (0.30, 0.54 and 0.69, respectively) and the Reynolds number, *Re* (-), being larger than 4000 (38000, 67000, 83000, respectively), calculated with:

$$Fr = \frac{u}{\sqrt{gh}} \tag{1}$$

$$Re = \frac{hu}{\nu} \tag{2}$$

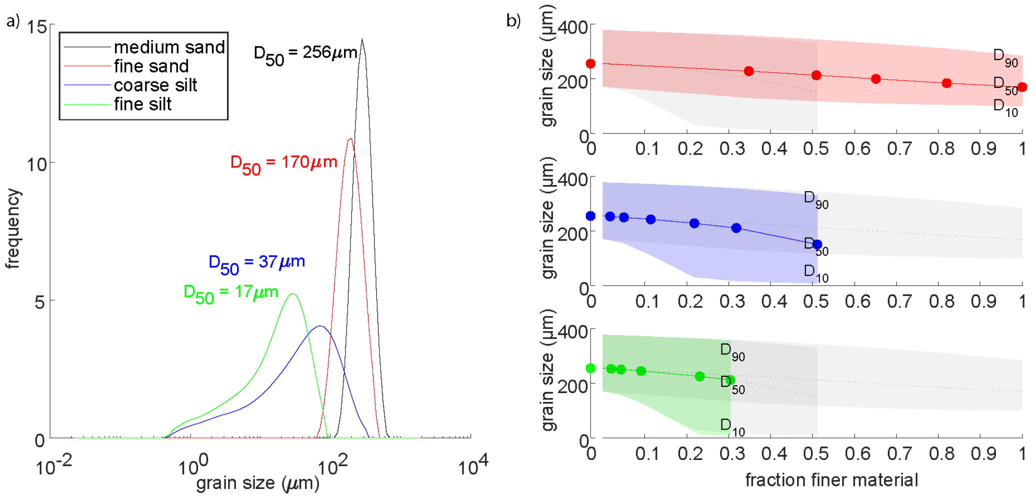

Figure 3. a) Grain-size distributions of the sediments used in the experiments. b) D_{10}, D_{50} and D_{90} of the tested mixtures, in which the finer material (fine sand, coarse silt or fine silt) is mixed with the base material (medium sand).

where u is the time and depth-averaged flow velocity (m s^{-1}), g is the gravitational acceleration (9.81 m s^{-2}), h is the water depth (0.15 m), and ν is the kinematic viscosity (m^2 s^{-1}), which is weakly dependent on water temperature, t (°C), as $\nu = 4 * 10^{-5}/(20 + t)$. Here, $\nu = 1.05 * 10^{-6}$ m^2 s^{-1} for 18 °C is used.

A sediment bed with a thickness of 0.10 m was applied, which consisted of a mixture of two grain sizes: a base sediment of medium sand (median size, $D_{50} = 256$ μm), mixed with fine sand ($D_{50} = 170$ μm), coarse silt ($D_{50} = 37$ μm) or fine silt ($D_{50} = 17$ μm) (Figure 3a, Supplementary Figure S1 for images of the sediment and Supplementary Figure S2 for all the grain size distributions). The sediments were mixed manually. All sediments were composed of silica (SiO_2). The particle size distribution of the four unmixed sediments was measured with a Mastersizer 3000 (Figure 3). The fine sand and coarse silt are non-cohesive, whereas the fine silt could be classified as weakly-cohesive (Wolanski, 2007), confirmed by visual observation of the sticky fine silt slurry and a significantly higher submerged angle of repose (40° instead of 30° for sand). No visible flocculation of the silt fraction occurred during the experiments.

The weight percentage of finer material mixed with the base material ranged from 0 to 100 wt% for fine sand, to 51 wt% for coarse silt (with 49 wt% medium sand) and to 30 wt% for fine silt (with 70 wt% medium sand). In total, 17 different mixtures were tested, which were all exposed to the low, medium and high discharge. In Table 1, an overview of the experimental mixtures is given. The D_{50} and 90th-percentile, D_{90}, values of the mixtures hardly changed when replacing part of the base material with coarse or fine silt, but the 10th-percentile, D_{10}, values dropped significantly (Figure 3b).

2.2 Instrumentation

A line laser and 3D camera (Figure 2f), equipped with Gigabit Ethernet (SICK, 2012), was used to scan the bed topography. The devices were mounted on a measurement carriage that moved on fixed rails along the flume. After every experimental run, the flume was slowly drained, and an area of 7 x 1 m was recorded in three parallel, partially overlapping, swaths, with a resolution of 0.1 mm. de Ruijsscher et al. (2018) provided a detailed description of the line laser scanner.

Table 1. Overview of the performed experiments. Seventeen different sediment mixtures were tested, in which the type and percentage of fine material relative to the base material (consisting of medium sand) varied per experimental run. Each experiment with a distinct mixture was conducted for low, medium and high discharge, resulting in 51 experiments. * the experiment with medium discharge was excluded from analysis because of clogging of the pumps.

experiment	% fine / % coarse
base experiment	
1	0/100
experiments with fine sand	
2-4	35/65*
5-7	51/49
8-10	65/35
11-13	82/18
15-18	100/0
experiments with coarse silt	
19-21	2/98
22-24	5/95
25-27	11/89
28-30	22/78
31-33	32/68
34-36	51/49
experiments with fine silt	
37-39	2/98
40-42	4/96
43-45	9/91
46-48	23/77
49-51	30/70

During the first and last 30 minutes of an experimental run, an UB-Lab 2C (UBERTONE) (Figure 2c) was deployed to measure flow velocity profiles. The UB-Lab 2C is an ADVP (acoustic Doppler velocity profiler, e.g. Hurther and Lemmin (2001) and Mignot et al. (2009)), which measures a two-component velocity profile at high spatial (1.5 mm) and temporal resolution, here 10 to 15 Hz. An acoustic signal is transmitted along a single beam and received by two receivers under different observation angles. The resulting 2-component vector is then projected to yield the 2-dimensional velocity in the streamwise direction (u) and vertical direction (w) along the beam (1D-profile). The emission frequency was set to 1 MHz with a bin size of 1.5 mm. The pulse repetition frequency ranged from 1200 to 1800 Hz for low and high discharge, respectively.

2.3 Data analysis

2.3.1 Sediment characterization

The behavior of the sediment in the experiments was estimated from the sorting of the sediment and the dominant way of sediment transport. This information was later used to interpret the observed bedform patterns.

The sorting was determined as:

$$\sigma_g = \sqrt{\frac{D_{84}}{D_{16}}} \tag{3}$$

To determine the dominant mode of transport, the Rouse number *Ro* (-) (Rouse, 1937) was calculated, which is the ratio between the settling velocity of a particle, w_s and the shear velocity, u^*:

$$Ro = \frac{w_s}{\kappa u^*} \tag{4}$$

in which κ is the Von Karman's constant (0.4), and the settling velocity of a particle was approximated with (Ferguson and Church, 2004; Dietrich, 1982):

$$w_s = \frac{\rho_r g D_{50}^2}{C_1 \nu + \sqrt{0.75 C_2 R g D_{50}^3}} \tag{5}$$

where ρ_r is the relative submerged density $= (\rho_s - \rho_w)/\rho_w$, and $C_1 = 18$ and $C_2 = 1$ for natural grains (Ferguson and Church, 2004).

If the Rouse number is larger than 3κ, the dominant transport mode is expected to be bedload, and if the ratio is smaller than 0.3κ, the dominant mode is expected to be suspended load (Dade and Friend, 1998). In between these values, the transport mode is mixed. The D_{50} of the four unmixed sediments was used, rather than the D_{50} of the mixtures, yielding a transport mode for the base sediment of medium sand and the finer fractions (fine sand, coarse and fine silt) separately. This approximation was verified by visual observation through a window in the side of the flume.

2.3.2 Bedform geometry

Final bed configurations were determined from the bed elevation data obtained with the line laser scanner. Five longitudinal transects were constructed across the width of the flume, with an interspacing of 200 mm. The resulting transects served as input for the bedform tracking tool of van der Mark and Blom (2007), which gives bedform geometry based on specific detrending lengths, used to differentiate between bedform scales. Based on spectral analysis, two bedform length scales were identified in our experiments: 150 ±

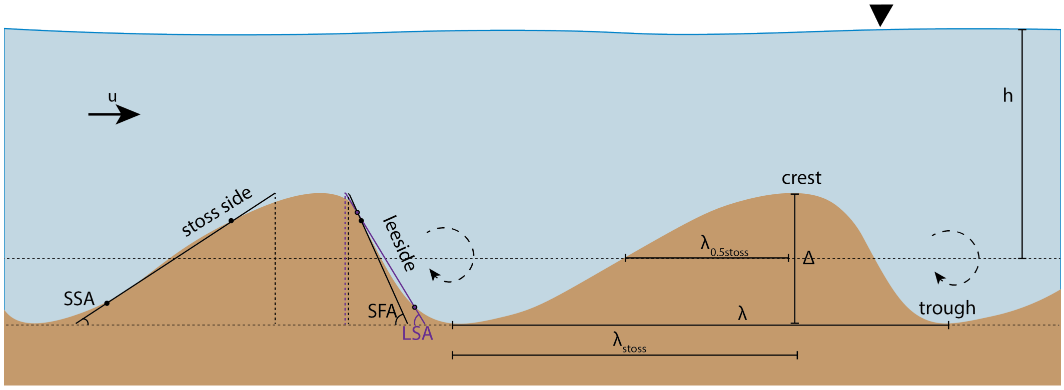

Figure 4. Definition of the bedform characteristics, showing the bedform height (Δ), the length (λ), the total length of the stoss side (λ_{stoss}) and the length of the stoss side at 0.5*Δ ($\lambda_{0.5stoss}$), the leeside angle (LSA), in which the upper and lower 1/6th of the leeside is excluded, the stoss-side angle (SSA), also excluding the upper and lower 1/6th of the stoss side, and the steep-face angle (SFA), which is the steepest part (95-percentile) of the leeside. The steepest part of the leeside is indicated with a small purple marker, and the location of the upper and lower 1/6th of the lee and stoss side are indicated with a small black marker.

100 mm (hereafter referred to as ripples), and 1100 ± 400 mm (referred to as dunes). Only if the bedforms occurred in at least two out of five profiles of a bed scan, bedform statistics were calculated.

Bedform characteristics (Figure 4) in this study included bedform height, Δ (m), the vertical distance between crest and downstream trough; bedform length, λ (m), the horizontal distance between two subsequent crests; leeside angle, LSA (°), the slope angle derived from a linear fit of the bedform's leeside, excluding the upper and lower 1/6 of the bedform height; stoss-side angle, SSA (°), calculated similarly to the leeside angle; and the steep-face angle (Lefebvre and Cisneros, 2023), SFA (°), the steepest part of the leeside, calculated as the 95-percentile of the distribution of angles along the leeside. The bedform roundness index, BRI, of the ripples was defined as the ratio between the length from the dune crest to the stoss side at 0.5 times the dune height ($\lambda_{0.5stoss}$) and the length of the stoss side (λ_{stoss}) (Perillo et al., 2014; Prokocki et al., 2022). A ripple was classified as rounded if $BRI \geq 0.6$. Finally, the ripple width, W (m), i.e. the horizontal distance between two subsequent "crests", was derived. For this, six cross-sectional profiles transverse to the flow were constructed, with an interspacing of 1000 mm. Next, the same bedform tracking tool was applied using the same detrending lengths as for the longitudinal profiles. The ripple width was calculated only for the low-discharge experiments, where the width of the bedforms was considerably smaller than the width of the flume.

2.3.3 Bedform geometry predictors

Various bedform geometry predictors were tested based on our data. The selected predictors for dune height and length included a measure of flow strength (van Rijn, 1984; Venditti and Bradley, 2022), and the predictor of Soulsby et al. (2012) was used for the height and length of ripples.

van Rijn (1984) developed an empirical dune height and length predictor, the former being dependent on the transport stage, T_{vRijn}, as measure of flow strength.

$$\Delta_{vRijn} = 0.11h\left(\frac{D_{50}}{h}\right)^{0.3}(1-e^{-0.5T_{vRijn}})(25-T_{vRijn}) \tag{6}$$

$$\lambda_{vRijn} = 7.3h \tag{7}$$

T_{vRijn} depends on shear stress and critical shear stress. See Appendix A for a full explanation.

Venditti and Bradley (2022) developed an empirical equation based on a different parametrization of transport stage, T_{VB}, defined as $\frac{\theta}{\theta_c}$, which is the ratio of the dimensionless shear stress, θ, and critical shear stress, θ_c. The equations suitable for laboratory flows with a water depth less than 0.25 m are:

$$\Delta_{VB} = h\left(-0.00100(\frac{\theta}{\theta_c} - 17.7)^2 + 0.417\right) \tag{8}$$

$$\lambda_{VB} = h\left(0.0192(\frac{\theta}{\theta_c} - 8.46)^2 + 6.23\right) \tag{9}$$

The geometry of ripples is only dependent on a measure of grain size (D^*) and independent of transport stage (Baas, 1994; Baas, 1999). According to the equations of Soulsby et al. (2012), their geometry can be predicted with:

$$\Delta_{Souslby} = D_{50}202D^{*-0.554} \tag{10}$$

$$\lambda_{Soulsby} = D_{50}(500 + 1881D^{*-1.5}) \tag{11}$$

All definitions and symbols are given in Appendix A.

2.3.4 Roughness characterization

Hydraulic roughness was estimated following two methods. Firstly, the measured velocity profiles were used, following the method of Hoitink et al. (2009). Secondly, an indirect hydraulic roughness predictor of van Rijn (1984) was used, based on bed geometry and sediment characteristics.

The first method is based on the Law of the Wall:

$$\frac{\overline{u}(z)}{u^*} = \frac{1}{\kappa}\ln(\frac{z}{z_0}) \tag{12}$$

where $\overline{u}$ is the time-averaged velocity (m s^{-1}) at height z above the bed (m), $\kappa = 0.4$ is the Von Karman constant, and z_0 is roughness length (m).

For a water column that satisfies equation (12), i.e. where the velocity profiles are logarithmic (Supplementary Figure S4), the shear velocity can be determined from the slope of the velocity versus dimensionless depth σ_d (equation (B2)). This, in turn, can be used to derive roughness length and, ultimately, Manning's n, n_{man} (s m$^{-1/3}$). See Appendix B for an elaborate definition. Experiments 13-18 were excluded from analysis, since erroneous mounting of the UB-Lab 2C caused invalid profiles.

Roughness was also approximated indirectly based on the predictor of van Rijn (1984). The total predicted hydraulic roughness, expressed as friction factor, $\hat{f}$, results from form friction and grain friction (Einstein, 1950). The total hydraulic roughness was predicted as in van Rijn (1984):

$$\hat{f} = \frac{8g}{(18\log(\frac{12h}{k_s}))^2} \tag{13}$$

where k_s is a measure of roughness both consisting of form roughness and grain roughness. See Appendix B for the corresponding equations.

Friction factor $\hat{f}$ can be converted to n_{man} via (Manning, 1891; Silberman et al., 1963):

$$n_{man} = \frac{R_h^{1/6}}{\sqrt{\frac{8g}{\hat{f}}}} \tag{14}$$

where R_h is the hydraulic radius, which is equal to the cross-sectional area (A) divided by the wetted perimeter (P = width + $2h$).

3 Results

3.1 Observed bed geometries

The bed geometries in the experiments were dependent on discharge (Figure 5a-c, see Supplementary Figures S3-S5 for the bed geometry of all runs), and on the fraction of fine material. Ripples were observed in the low-discharge experiments, whilst dunes were observed in the medium and high-discharge experiments, and the bedform tracking tool was applied accordingly. Below, we show the results separately for low, medium and high discharge.

3.1.1 Low discharge bedform geometries

At low discharge, only ripples appeared on the bed (Figure 5a, c). The ripples had an average height of 0.011 m, an average length of 0.12 m and a non-rounded shape with a steep-face angle of 22°.

Ripple height and width both decreased with an increasing fraction of coarse silt and fine silt, which is especially pronounced at a silt percentage above 20% (Figure 6a, c). The ripple height decreased up to 38% for coarse silt and 28% for fine silt compared to the experiment with pure medium sand. The corresponding decrease in length was considerably smaller (up to 14% and 4%, respectively). This decrease in ripple height was not visible in the experiments with fine sand. The *LSA* and *SFA* of the ripples were less dependent of the type and percentage of finer material (Figure 6c,d). Ripple width decreased up to 11% and 23% for coarse and fine silt, indicating that the ripples became more three-dimensional in shape. Finally, the *BRI* had a near-constant value of 0.42, indicating non-rounded ripples.

3.1.2 Medium discharge bedform geometries

The bedforms generated during medium discharge were dunes, which were generally larger than those that emerged during low discharge, with an average height of 0.027 m, a length of 0.54 m, and a slightly lower steep-face angle of 20°. The dunes followed two general trends. Firstly, the runs with an increasing amount of fine sand and coarse silt showed an increase in dune height and length (Figure 5b). Especially for the coarse-silt runs, the increase in dune length was considerable (Figure 7b). The dune length in these runs was on average 0.59 m for the experiments with 20% coarse silt or less, and increased to 1.1 m for the experiments with a higher coarse-silt percentage in the bed (86%). This increase in dune length was accompanied by a smaller increase in dune height from 0.032

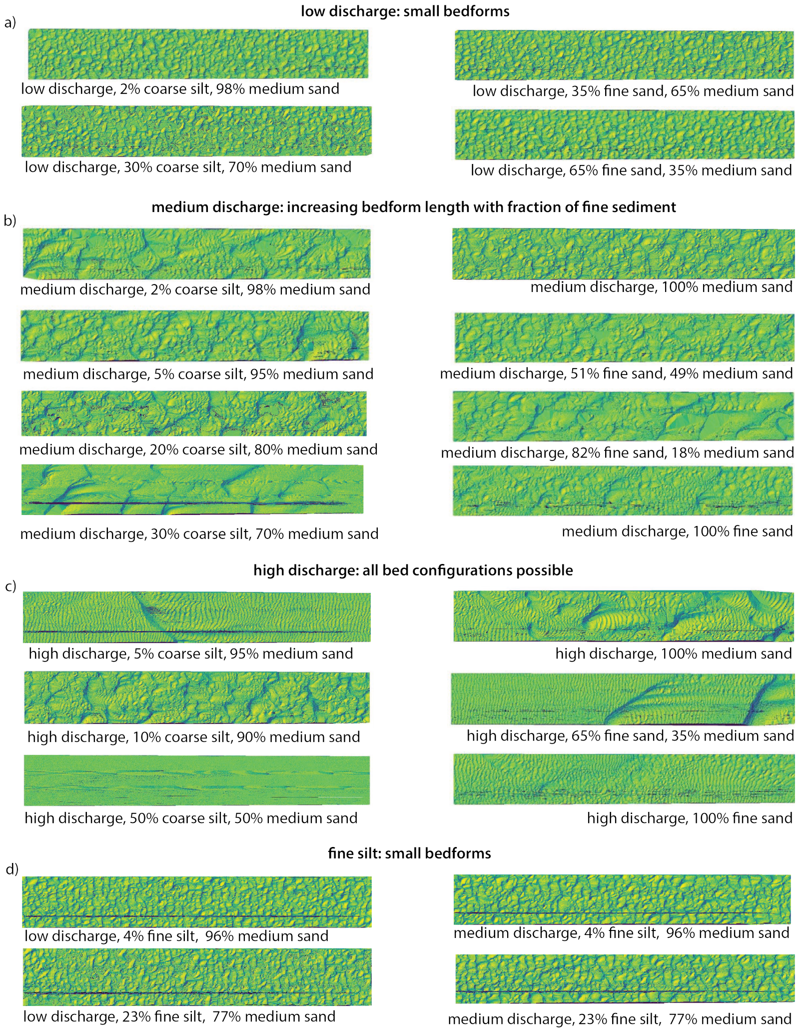

Figure 5. Dynamic equilibrium bed morphologies at the end of selected experiments. All images represent a 1 m wide and 7 m long section of flume. a) Ripples at low discharge. b) Dunes at medium discharge, showing increasing dune length with increasing finer material. c) Bed morphologies with large variability at high discharge. d) Impact of fine silt on bed morphology. Scans in (c) show small two-dimensional ripples superimposed on larger bedforms and flat beds. These ripples are artifacts caused by draining the flume over an almost flat bed (see Supplementary Figure S6 for verification).

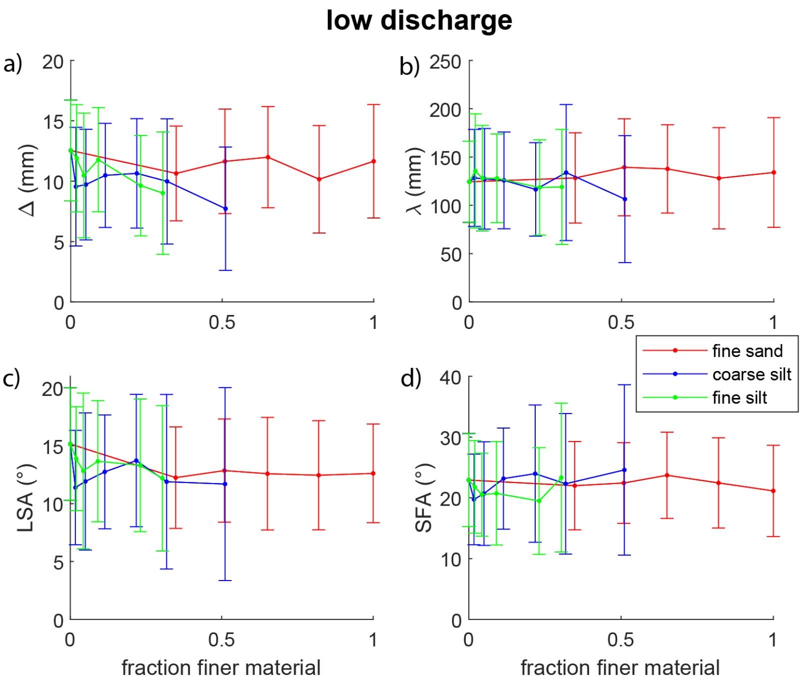

Figure 6. Bedform geometries at low discharge (45 L s^{-1}). a) Bedform height. Δ. b) Bedform length, λ. c) Leeside angle, *LSA*. d) Steep-face angle, *SFA*. The error bars indicate the standard deviation.

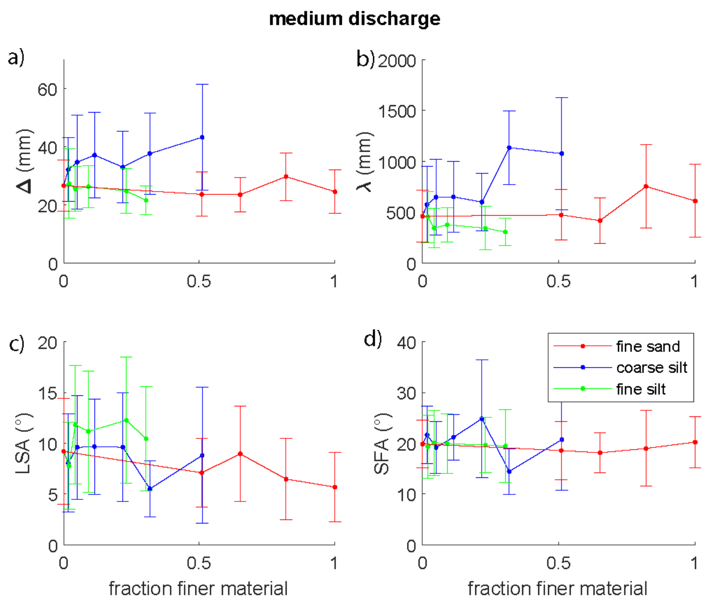

Figure 7. Bedform geometries at medium discharge (80 L s^{-1}). a) Dune height, Δ. b) Dune length, λ. c) Leeside angle, *LSA*. d) Steep-face angle, *SFA*. The error bars indicate the standard deviation

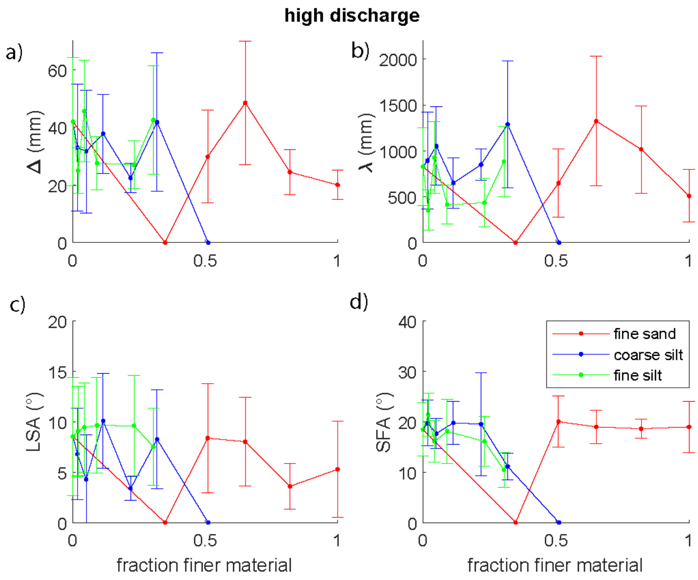

Figure 8. Bedform geometries at high discharge (100 L s^{-1}). a) Dune height, Δ. b) Dune length, λ. c) Leeside angle, LSA. d) Steep-face angle, SFA. Zero values indicate a flat bed, the error bars indicate the standard deviation.

m to 0.043 m (34%; Figure 7a). Dune heights and lengths for the experiments with fine sand were smaller than for the experiments with coarse silt (on average Δ = 0.026 m and λ = 0.54 m for fine sand, and Δ = 0.035 m and λ = 0.73 m for coarse silt). The leeside angles varied per experiment, but the steep-face angles remained relatively constant, lacking a consistent trend with increasing content of fine material (Figure 7c and d).

The experiments with fine silt showed smaller dunes compared to the coarse silt and fine sand experiments. However, they were larger than the ripples found in the low-discharge experiments, and comparable in planform shape (Figure 5a, d). The mean dune length was 0.38 m, which is significantly smaller than for the experiments with fine sand and coarse silt. However, at 0.025 m, the mean dune height is comparable to the runs with fine sand. A decrease in length and height was observed for the runs with 0 to 30% fine silt (23% decrease in dune height, 51% decrease in dune length). Leeside angles were 28% larger than in the experiments with fine sand and coarse silt, but the steep-face angles were comparable.

3.1.3 High discharge bedform geometries

The dunes formed at high discharge were on average slightly larger than during medium discharge (Figure 8), with an average height of 0.029 m and length of 0.72 m. The steep-face angle was 18°, which was slightly lower than at medium discharge. However, the geometrical parameters were highly variable, and the high discharge experiments showed a standard deviation of 1.6 cm, 39 cm, 4.6° for dune height, length and steep-face angle, respectively, and without a clear relationship with the amount of fine material. The experiments with fine silt resulted on average in shorter dune lengths and higher leeside angles than the experiments with coarse silt and fine sand, which agrees with the observations at medium discharge.

The high discharge experiments were conducted close to the suspension threshold (Ro $< 0.3\kappa$), and the dunes started to wash out towards upper stage plane bed, when three

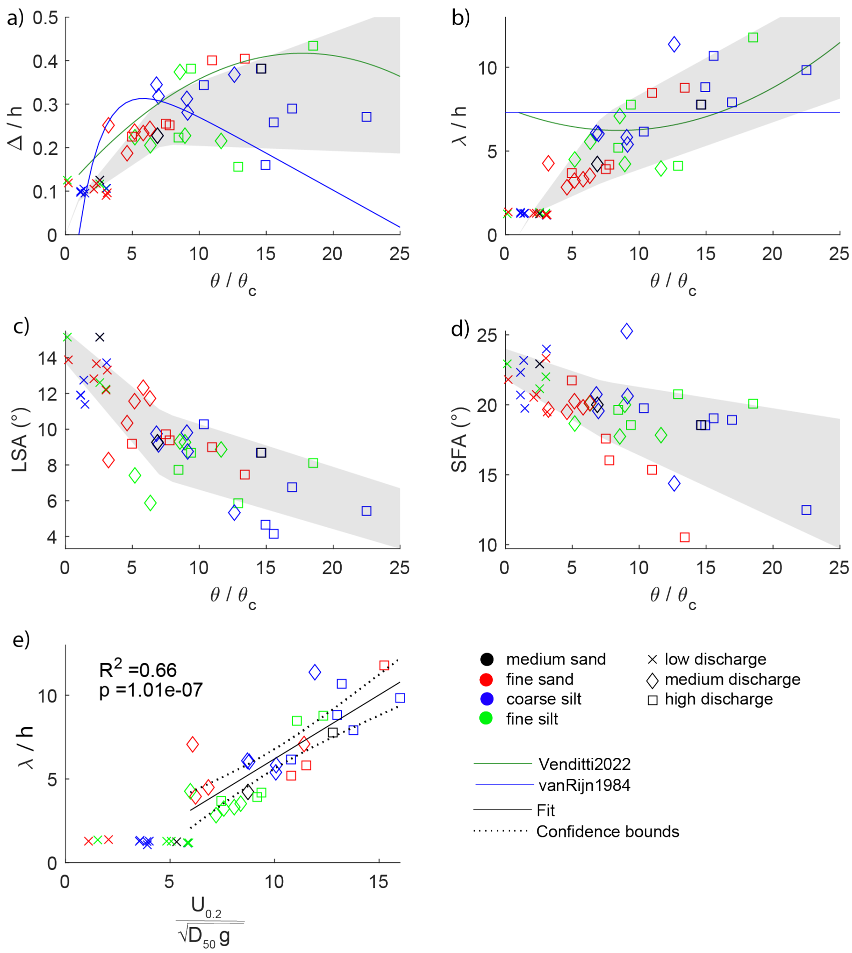

Figure 9. Increasing variability in bedform geometry with increasing flow strength, expressed as transport stage (θ/θ_c) in (a-d) and as non-dimensionalized velocity at 20% above the bed in (e). a) Bedform height divided by water depth. b) Bedform length divided by water depth. c) Leeside angle. d) Steep-face angle. e) Bedform length divided by water depth. Grey shading indicates one standard deviation from the mean value, in which the standard deviation is calculated from all bedforms in either low, medium or high discharge experiments. The base runs are indicated with black markers (medium sand). In (a) and (b), the predicted values by Venditti and Bradley (2022) and van Rijn (1984) are shown.

different bed states were observed (Figure 5c): an almost flat bed with one or two large, steep bedforms; a bed covered with dunes; and a flat bed.

3.2 Bedform variability

Relationships between dune geometry and transport stage, θ/θ_c, are evident from the experimental data (Figure 9). Dune length increased, and leeside and steep-face angle decreased with increasing transport stage, whereas the relationship between dune height and transport stage approached a parabola (Figure 9a-d). No relation between ripple geometry and transport stage is apparent. Additionally, the variability in bedform dune geometry increased with increasing transport stage, indicated by the gray shaded band in Figure 9a-d.

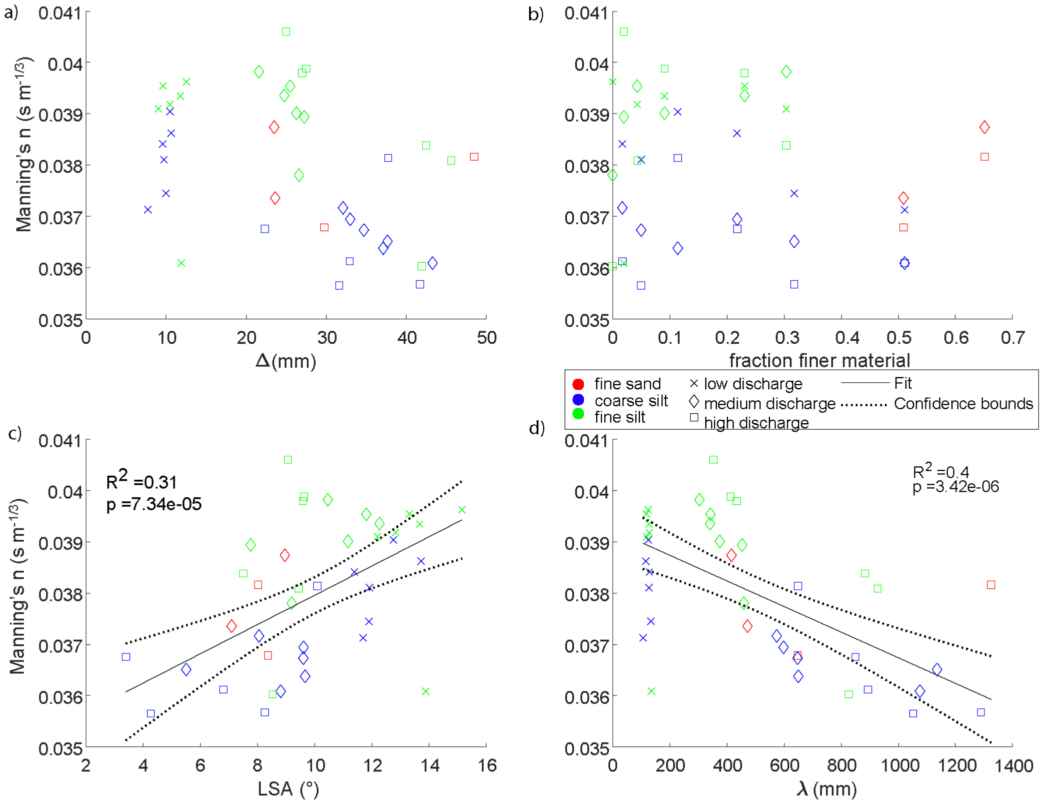

Figure 10. The relation between the hydraulic roughness n_{man}, calculated with the Law of the Wall, and a) Bedform height, Δ. b) Fraction finer material within the base material. c) Leeside angle, LSA. d) Bedform length, λ. Significant linear relations are shown in c and d.

The near-bed velocity $U_{0.2}$, which is the time-averaged velocity at the dimensionless height above the bed of $\sigma_d = 0.2$ and directly measured with the UB-Lab 2C, is a representation of the near-bed conditions influencing and being influenced by the bed geometry. The near-bed velocity shows a strong relation with the dimensionless dune length ($R^2 = 0.66$) (Figure 9e).

The bedform height and length predictions for dunes based on van Rijn (1984) and Venditti and Bradley (2022) are shown in Figure 9a-b. For the low-discharge runs, the ripple predictor of Soulsby et al. (2012) performs relatively well, with root-mean-square errors of 0.001 m for height and 0.02 m for length. For the medium and high discharge runs, the dune predictor of van Rijn (1984) performs reasonably well for medium transport stages, but it mostly underpredicts dune heights for high transport stages. The predictor of Venditti and Bradley (2022) slightly overpredicts dune height, but the measured values are still within their margins of error. The dune length predictor of van Rijn (1984), which is purely based on water depth, does not capture the trend of increasing dune length with increasing transport stage. The predictor of Venditti and Bradley (2022) largely overestimates dune length for medium transport stages. For the high transport stages it captures the observed increase in dune length better compared to the dune length predictor of van Rijn (1984).

3.3 Hydraulic roughness

Hydraulic roughness, expressed as the depth-independent Manning's n and calculated via the Law of the Wall based on the velocity profiles (equation (12)), averaged 0.038. n_{man} increased with increasing leeside angle ($R^2 = 0.31$) and decreasing bedform length ($R^2 = 0.40$) (Figure 10c-d). The relation with leeside angle stands out (Figure 10c), since the ripples (indicated with 'x') and dunes (indicated with squares and diamonds) are both part of the linear correlation between leeside angle and roughness, whereas no relation between ripple length and roughness was observed. Generally, the roughness was larger during the experiments with fine silt (Figure 10) and during the experiments with a rippled bed. The larger roughness is likely to be related to shortening of the bedforms and the associated relatively high leeside angle of the bedforms observed in those experiments. Vice versa, for the experiments where coarse silt was added, Manning's n was conistently lower, which relates to lengthening of the bedforms and flattening of the LSA.

When lumping all data in a single dataset, those relations between hydraulic roughness, dune height and the fraction of finer material are lost (Figure 10a-b). Such a lack of a relationship with fine material is consistent with the roughness predictor of van Rijn (1984) (equation 13), which differentiates between skin friction, related to grain size, and form friction, related to bedform size. According to this predictor, on average, 97% of the total amount of friction is attributed to form friction in the experiments, indicating that bed composition is less important for hydraulic roughness than bedform geometry. The roughness predictor of van Rijn (1984) yields on average a Manning's n of 0.030, which is 11% lower than the measured friction based on the Law of the Wall. Our results suggest that depending on the grain size, a small fraction of fine material influences hydraulic roughness by influencing the bedform geometry.

4 Discussion

4.1 A shift in transport stage due to the presence of fines

The transport stage-based dune height predictor of Venditti and Bradley (2022) provides a way to visualize the experimental results and assess deviations from expected bedform heights caused by adding fine sediment (Figure 11). The predictor implies a parabolic relationship between dune height and transport stage, as well as confidence levels for data variability (Bradley and Venditti, 2017). The parabolic relation can be interpreted as follows. As the transport stage increases, the transport mode changes from bed load to mixed load, and dune height increases. This corresponds to our low and medium-discharge experiments. As the transport stage increases further, dunes start to become washed-out, thus reducing the dune height. This corresponds to our high-discharge experiments (Yalin, 1972; Naqshband et al., 2014).

Although this framework is generally associated with a change in flow strength (Shields number, θ), it can also be used to frame the experimental data using changes in sediment mobility (critical Shields number, θ_c) caused by the replacing some of the coarse base sediment with fine material (Figure 11). During the medium-discharge experiments, non-cohesive fine sand and coarse silt led to an increase in dune height and length. When comparing this to the expected change based on the predictor of Venditti and Bradley (2022) due to a decrease in D_{50} resulting from the presence of fine sediment, the change in dune geometry was larger than expected. We suggest that the increase in dune size is caused by an increase in mobility of the bed material (i.e. a decrease in θ_c), leading to a larger change in transport stage (Section 4.2) than expected based on the change in D_{50} (Supplementary Table S1). Therefore, the presence of fine, non-cohesive material in the base material leads to a shift to the right on the dune height - transport stage diagram (Figure 11). In contrast, the presence of fine, weakly cohesive material may decrease the mobility of the sediment (Section 4.3), and therefore decreases the transport stage, resulting in a decrease in dune size, leading to

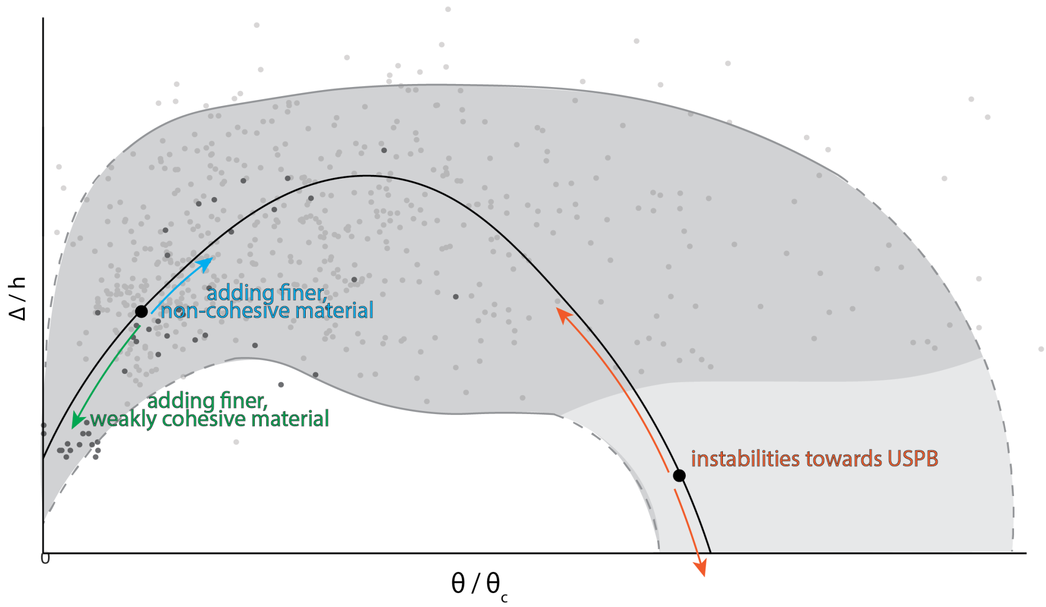

Figure 11. Conceptual diagram of non-dimensionalized dune height against transport stage, indicating the impact of the presence of non-cohesive and cohesive fine sediment in the bed at relatively low transport stages, and the increased variability of bedform height due to flow instabilities at high transport stages. The dark gray shading indicates the 5 and 95-percentiles of data aggregated from Venditti et al. (2016) and Bradley and Venditti (2019). Data from this study are shown with dark gray markers. No data are available for the light gray shaded area. The dashed lines show the estimated course of the confidence intervals.

a shift to the left on the diagram in Figure 11. Furthermore, the large variability in dune geometry at the high transport stages may be attributed to instabilities that occur when the system moves towards upper-stage plane bed (Section 4.4). Finally, the ripples formed at low discharge do not fit within the transport stage diagram, since ripple size is only dependent on grain size and not on flow velocity (Baas, 1994; Baas, 1999; Soulsby et al., 2012). Below, these changes are discussed in more detail.

4.2 Impact of non-cohesive fine sediment (fine sand and coarse silt)

4.2.1 Hiding-exposure effect

During the medium-discharge experiments, we observed an increase in dune size with larger fractions of fine non-cohesive material (fine sand and coarse silt) mixed into the base material. This may be attributed to an increased mobility of the coarse sediment. Sediment grains in heterogeneous sediment mixtures interact with the flow and with each other in a different way than in homogeneous sediment mixtures (McCarron et al., 2019), leading to selective entrainment. This is called the hiding-exposure effect, where small grains are hidden from the flow between the coarser grains. This does not only result in a more difficult mobilization of the fines (hiding), but also in an increased mobility of the larger grains (exposure) (Einstein, 1950) (see Section 4.2.2).

The hiding-exposure effect is mostly dependent on the ratio between the fraction of interest D_i (here, the coarse fraction) and the D_{50}. Hill et al. (2017) tested the influence of this ratio for gravel-sand mixtures. They found that if the two mixed sediments had similar grain sizes, (D_{coarse} / $D_{fines} < 2$), no preferential mobilization of the coarser fraction took place, and the fines became part of the bed structure (Frings et al., 2008). For intermediate particle ratios ($2 < D_{coarse} \ / \ D_{fines} < 20$), the fine sediment filled or bridged the pores of the coarser base matrix, resulting in increased mobility of the coarse fraction (Section 4.2.2). For large ratios ($D_{coarse} \ / \ D_{fines} > 20$), the fine sediment percolated through the base sediment of medium sand. The subsurface became clogged, but the fines were not present in the surface layer, because all free fines were entrained and transported in suspension.

In the present experiments, the ratios between the coarse and fine fractions were 1.5, 6.9 and 15 for fine sand, coarse silt and fine silt, respectively. Following Hill et al. (2017), this implies that the fine sand might have aggregated the bed structure, whereas the coarse and fine silt bridged or filled the pores of the coarse fraction. For the silts, the hiding-exposure effect is expected to have increased the mobility of the coarse fraction. For the fine sand, however, the increased size distribution might have resulted in increased mobility of the entire sediment bed due to an increase in grain protrusion and a decreased friction angle (Kirchner et al., 1990; Buffington et al., 1992). This effect may have been smaller than the mobility increase caused by the hiding-exposure effect by coarse silt, which is indicated by the increased lengthening of dunes in a bed with coarse silt compared to fine sand (Figure 7). Increased mobility means an increased transport stage, hence an increased dune length (Section 4.1).

Various methods have been developed to correct the initiation of motion of sediments for the hiding-exposure effect (see McCarron et al. (2019) for a review). Generally, the correction factor lowers the critical Shields number, θ_c, for the coarse fraction ($D_i > D_{50}$), and increases it for the fine fraction ($D_i < D_{50}$). The correction factor, ζ, commonly takes this form (Einstein, 1950; Wilcock, 1993):

$$\zeta = \alpha \left(\frac{D_i}{D_{50}} \right)^{-\beta} \tag{15}$$

where D_i is the grain size of the fraction of interest, β controls the strength of the hiding-exposure effect (Buffington and Montgomery, 1997; McCarron et al., 2019), and $\alpha = 1$ for sediments with the same density. Exponent β has been approximated using σ_g (Equation 3), as a measure for sorting (Patel et al., 2013; McCarron et al., 2019): $\beta = 0.96$ for $\sigma_g < 2.85$ and $\beta = 2.67\mathrm{e}^{-0.37\sigma_g}$ for $\sigma_g \geq 2.85$, where σ_g is determined with equation (3).

Applying this correction factor to the experimental data shows that a larger fraction of fine material results in a larger increase in mobility of the coarse material (Supplementary Figure S8). For example, replacing 50% of the base material by fine sand causes θ_c of the base material to decrease from 0.021 to 0.019 (-11%) and to 0.016 for 50% coarse silt (-31%) (Supplementary Table S1). Applying this adjusted critical Shields number to our data reduces the root-mean-square error (RMSE) of the observed normalized dune height by 0.019 (-9%) and 0.032 (-15%) for fine sand and coarse silt, respectively, when evaluated against the predictor of Venditti and Bradley (2022). In contrast, the same adjustment increases the RMSE for the experiments with fine silt by 0.011 (+6%) and causes the variability for the high discharge runs to remain high, with a RMSE of 0.31.

4.2.2 The hiding-exposure effect in mixed gravel-sand and sand-silt beds

The hiding-exposure effect is not commonly recognized in studies focused on sand-silt mixtures, and is mainly based on experiments in gravel-sand mixtures. McCarron et al. (2019) described an increase in mobility in gravel-sand experiments based on a decrease in θ_c by 64% compared to well-sorted sediment of a similar size (2.14 mm). Frings et al. (2008) speculated that hiding-exposure could result in a more mobile coarse fraction than a fine fraction in the downstream part of sand-bed rivers. Our observations with sand-silt mixtures show parallels to gravel-sand mixtures, but on a smaller grain-size scale. We therefore infer that the hiding-exposure effect could also play a role in sand-silt mixtures.

Mechanisms explaining the increased mobility of gravel in sand-gravel mixtures were suggested by Ikeda (1984) and subsequently built on in later studies (e.g. Li and Komar 1986; Whiting et al. 1988; Dietrich et al. 1989; Wilcock 1993; Venditti et al. 2010). Firstly, by filling pores with fine grains, the pivoting angle of large grains is reduced, thus facilitating entrainment (Li and Komar, 1986). Secondly, there is a lower probability that particles in transport are caught in the wake of protruding particles and deposit, since particles protrude less far into the flow. Finally, filling pores with fine material results in a smoother bed, thus resulting in lower drag, which in turn increases the near-bed velocity. These suggestions were built upon by Venditti et al. (2010), who suggested that the infilling of the pores causes dampening of small wakes in the lee of particles, resulting in acceleration of the near-bed flow, which in turn mobilizes the larger particles. Our experimental results suggest that this acceleration of near-bed velocity is reflected in an increase in dune length and height at medium discharge (Figure 9d), which is in agreement with the study by Yager et al. (2018), who suggested that time-averaged local flow velocity is strongly related to the time-averaged local bedload flux.

The hypothesis that the sediment mobility increases with an increased coarse silt fraction is in line with what can be expected from experiments with gravel-sand mixtures, but opposes previous observations in laboratory experiments with sand-silt mixtures. Bartzke et al. (2013) and Yao et al. (2022) observed that non-cohesive silt stabilizes the sediment bed, but at different concentrations ($\sim$1.4% silt and >35%, respectively). In our experiments, even at 50% coarse silt the mobility of the sediment was increased. Interestingly, Bartzke et al. (2013), whose experiments fall in the range of pore bridging (D_{coarse} / D_{fines} = 5.5), explained the filling of pore space as a reason for increased stability of the bed due to reduced hyporheic flow, rather than a reason for increased mobility of the coarse fraction as found in gravel-sand experiments (Section 4.2.1). The reason for these opposing effects could lie in the different experimental setups: the highest flow velocity tested in these experiments was 0.35 m s^{-1}, which is comparable to our lowest flow velocity. It is therefore likely that the stabilizing effect of silt, as observed in the studies of Bartzke et al. (2013) and Yao et al. (2022) may not be strong enough to continue stabilizing the bed when subject to higher shear stresses such as in our study.

Ma et al. (2020) studied the mobility of silt-sized sediment and the effects of sorting in laboratories and rivers world-wide, and found a high-mobility sediment transport regime related to the size and sorting of the bed sediment. Bed sediments of $D_{50} < 88$ μm and poorly sorted sediments within a range of 88 μm $< D_{50} <$ 153 μm were found to be more mobile than expected from the sediment transport rate equations of Engelund and Hansen (1967), whereas both well and poorly-sorted sediments with $D_{50} >$ 153 μm confirmed these equations. In other words, poorly sorted sediments in the transitional range of very fine to fine sand are more easily mobilized than narrowly distributed sediments. This agrees with equation (15), where the strength of the hiding-exposure effect is related to the sorting of the material. Although Ma et al. (2020) did not explicitly mention the hiding-exposure effect, and related their observation to the change from mixed load to suspended-load dominated transport, the hiding-exposure effect may have played a role to achieve this change.

4.3 Impact of weakly cohesive fine silt

Contrary to the increase in mobility observed when non-cohesive fine material was present, the replacement of the base sediment with fine silt reduced both the height and length of the bedforms. This might be attributed to the weakly cohesive character of the 17 μm-sized silt, because cohesive sediments such as clay are known to limit or suppress bedform growth (Schindler et al., 2015; Parsons et al., 2016) through London-van der Waals forces and by interparticle electrostatic bonding (Mehta, 2014), consequently increasing θ_c.

The fine silt used in our experiments exhibited weakly cohesive properties, confirmed by visual stickiness of slurries of the fine silt and an increased angle of repose. Therefore, fine silt might have imparted similar attractive forces as clay, although to a lesser extent. Schindler et al. (2015) and Parsons et al. (2016) performed experiments with fine sand (D_{50} = 239 μm) at a mean velocity u = 0.8 m s^{-1}, and observed an inverse linear relationship between dune height and clay percentage, with a lack of dunes at a clay percentage of 15%. The sharp decline in bedform height with clay content observed in their experiments was not evident in the present experiments, and the bed remained mobile up to 30% fine silt. Nevertheless, in the medium-discharge experiments, the dune heights and lengths for fine silt were significantly reduced, as opposed to the increase for coarse silt and fine sand, likely due to decreased mobility of the entire bed. In the low-discharge experiments, the ripple size was reduced too, but, as shown below, this could be a result of decreased grain size rather than decreased mobility.

Wu et al. (2022) recorded a decrease in ripple height with increasing clay percentage under wave-current conditions (D_{coarse} / D_{fines} $\sim$ 51). Below 11% clay, the clay was winnowed out of the bed, allowing clean-sand ripples of similar size to develop. Above 11%, the cohesiveness of the bed was large enough to limit bed mobility, and only small ripples formed. In our experiments, this effect did not occur, as even at small percentages of fine silt ($\sim$ 2%) bedform height decreased, as in the current-ripple experiments with mixed clay-sand of Baas et al. (2013). During the medium-discharge experiments, cohesion impeded dune formation, and only small dunes formed. In the high-discharge experiments, dunes did form, but their planform was more similar to the dunes formed in the medium-discharge experiments with fine sand and coarse silt than to those in the high-discharge runs (Supplementary Figure S3 and S4), suggesting cohesion-induced hampered mobility.

In summary, the formation of relatively small bedforms in our experiments with fine silt might be attributed to reduced mobility, caused by the weakly cohesive properties of fine silt. This effect is less pronounced than in previous experiments with more strongly cohesive clay, in which the mobility was limited more strongly. The decreased mobility leads to an increase in the critical Shields number, and a shift to lower θ/θ_c-values in Figure 11.

4.4 Instabilities at high discharges

Figure 11 shows that the variability in relative dune height increases with transport stage. High variability may dwarf any impact of fine sediment on bed geometry, and encompasses three bed configurations, without any apparent relationship with the type or fraction of fines: a dune-covered bed; a flat bed with one large dune (cf. Saunderson and Lockett (1983) and Naqshband et al. (2016)); and a completely flat bed. Based on previous studies (Venditti et al., 2016; Bradley and Venditti, 2019; Saunderson and Lockett, 1983), part of this variability lies in temporal changes in bed geometry.

The variability in dune geometry and the presence of multiple bed configurations have been described before in literature. Saunderson and Lockett (1983) performed experiments around the transition from dunes to upper-stage plane bed and found four different bed states: asymmetrical dunes; convex dunes; humpback dunes (comparable to the single large dune configuration in this study); and a flat bed.These bedform states were seen to transform into one another. Saunderson and Lockett (1983) dedicated this behavior to the close position of the bed to the phase boundary between dunes and upper-stage plane bed, but did not provide a physical explanation. Venditti et al. (2016) observed three phases in high-velocity experiments: a plane bed with washed-out dunes; a field of large dunes; and a field of small dunes. The water depth, shear stresses and water surface slope co-varied with the changes in bed configuration. During the plane-bed phase, intense localized erosion was followed by the formation of ripples or dunes, which then washed out to form a new flat bed. These cycles lasted from several minutes to more than half an hour, with transitions between individual bedform types happening in seconds or minutes. Similarly, Bradley and Venditti (2019) stated a 'tremendous variability' between bed states at a high transport stage, and reasoned that numerous observations of the bed are needed to get an average bed state that scales with the transport states described by equations (8) and (9).

However, none of these studies provided an explanation for the large variability in dune height at high transport stages. de Lange et al. (2024) reanalyzed the data of Venditti et al. (2016) and Bradley and Venditti (2019), and found a bimodal dune height distribution at high transport stages. They attributed this to a critical transition, suggesting flickering between a high and low alternative stable state. Our current observations fit within this alternative stable states framework, although proof is lacking due to the absence of temporal data. The large variability in bed configurations could explain the lack of a predictable succession of bed states with increasing amounts of fine sediment in the current study.

4.5 Ripples at low discharges

Ripples formed in the low discharge experiments. Ripple height and length are a product of the size of the bed material, and are independent of flow velocity (Baas, 1994; Baas, 1999; Soulsby et al., 2012). Therefore, the transport stage framework as suggested above for dunes is not relevant for ripples. The height and width of the ripples, and to a lesser degree their length, decreased with an increasing amount of coarse and fine silt. The decrease in height is most apparent at silt concentrations above 20%, the same percentage at which the D_{10} of the sediment distribution drops considerably (Figure 3).

Changes in ripple geometry as observed in the experiments are largely as expected. Replacing part of the base material with fine sand led to a decrease in height of about 15%, a similar decrease as expected based on Soulsby's ripple predictor (equation 10). This suggests that the change in grain size dominated the change in ripple height, and the effect of grain size was greater than any possible effect of hiding-exposure. However, coarse silt in the base material had a larger decreasing effect on height and length than fine sand. This may be caused by three processes; a) a mobility increase induced by the hiding-exposure effect; b) a shorter equilibrium time for coarse silt ripples at the same Shields stress; c) a larger relative effect of coarse silt than fine sand, as a 50% increase in weight of the finer fraction involves a much larger number of coarse silt than fine sand particles (in the same volume, there are 331 times more coarse silt particles than medium sand particles, as opposed to 3 times for fine sand). Finally, replacing part of the base material with fine silt shows the effect of cohesion of the fine silt by reducing the ripple height. However, the effect of particle size cannot be distinguished with confidence from that of cohesion. The decrease in ripple height with increasing fraction of fine silt is larger than for coarse silt, which might be at least partly caused by the cohesive properties of the fine silt.

4.6 The impact of bed sediment on hydraulic roughness

We confirm that for relatively steep dunes, roughness is related to the steepness of the leeside, consistent with findings of Kwoll et al. (2016) and Lefebvre and Winter (2016). At the leeside of the dune, flow separation generates turbulence, resulting in energy dissipation in the turbulent wake, which constitutes the main source of dune-related roughness (Lefebvre et al., 2014; Venditti and Bennett, 2000). In our experiments, the bedforms had on average a leeside angle of 10° with a relatively steep section (mean steep-face angle 20°), which should result in intermittent flow separation following Lefebvre and Cisneros (2023). The presence of flow separation can also be determined using the defect Reynolds number (Baas and Best, 2000), Re_d ($Re_d = \frac{\Delta u^*}{\nu}$). In all our experiments, Re_d is far larger than 4.5, which indicates the presence of flow separation (Williams and Kemp, 1971; Best and Bridge, 1992; Gyr and Müller, 1996).

Previous research suggested that the composition of the sediment bed has only a small influence on hydraulic roughness (Smith and McLean, 1977). This corresponds with our findings and equation (13) as far as skin friction is concerned; only 3% of the total roughness is attributed to skin friction in the present experiments. The bed composition does impact the dune geometry, thereby influencing form roughness (Figures 9e and 10d). Our results show bedforms respond differently to the type of finer material added. Bedform length decreased with an increasing fraction of fine silt, while it decreased with an increasing fraction of coarse silt. The indirect relation between bed composition and roughness is therefore only visible when looking at the resulting bedform characteristics.

4.7 Wider implications

It is inferred from our results that the presence of fines affects sediment mobility, even if the fines only slightly change the D_{50} of the sediment. Therewith, fine material influences bedform properties and hydraulic roughness, which is worth accounting for in bedform size predictors. Moreover, the interaction of fine silt and sand with coarser sand is relevant for channel nourishment aimed at preventing channel incision (Czapiga et al., 2022).

To adequately determine bedform geometry, some measure of bimodality or sorting may be included in future predictors. This measure could focus on the fine fraction, such as the D_{10}. Additionally, the bed geometries with fractions of fine and coarse silt differ notably, if the fine silt fraction is cohesive. Hence, assessing the cohesive properties of silt, such as yield stress and viscosity, is crucial, and lumping fines into one fraction, with a cut-off at 63 μm (e.g. van Rijn (2020)) is to be avoided.

5 Conclusions

We performed 51 laboratory experiments, in which the bed composition was varied using three different sediment mixtures (medium sand with fine sand, coarse silt and fine silt) in different ratios, for three different discharges (low, medium, high). We measured the bed morphology at the end of the experiments to assess the effect of bed composition on bedform geometry, and used this to indirectly assess sediment mobility and transport stage.

Bedform response to an increasing fraction of fine material depends, among others, on transport capacity, bimodality-impacted bed mobility, and cohesion. In the dune regime, the presence of fine sand or coarse silt in medium sand leads to an increase in dune length, and an increase or decrease in dune height, depending on the initial value of θ/θ_c. This may be attributed to an increase mobility of coarser material, leading to an increase in transport stage. The increase in mobility of medium sand is inferred to be caused by the hiding-exposure effect, with the filling of pores by coarse silt leading to a larger near-bed flow velocity. Fine sand is too coarse to fit in the pores, which causes an increase in grain protrusion and a decrease in friction angle. This may be more important than the hiding-exposure effect, but nevertheless lead to an increased sediment mobility .

The presence of weakly cohesive fine silt in medium sand has a similar effect to cohesive clay (Schindler et al., 2015) by inhibiting dune growth, possibly caused by a decrease in transport stage. In the ripple regime, an increased fraction of fine material leads to a decrease in ripple height, which responds directly to the decreased particle size. In the transitional regime from dunes to upper-stage plane bed, many different "equilibrium" bed geometries are observed. This complicates the relation between bedform geometry and fine sediment fraction. The observed variety in bed states fits within the framework of alternative stable bed states, where multiple bed geometries can form at high flow. The composition of the sediment bed does not significantly influence hydraulic roughness from skin friction drag, but alters the bed morphology, and thus indirectly changes the hydraulic roughness by altering form drag.

Appendix A Bedform geometry predictors

The dune height and length predictions based on van Rijn (1984) follow equation (6) and (7) in which T is van Rijn (1984)'s definition of the transport stage.

$$T_{vRijn} = \frac{(u^*)^2 - (u_c^*)^2}{(u_c^*)^2} \tag{A1}$$

where u^* is the shear velocity (m s^{-1}), and u_c^* is the critical shear velocity (m s^{-1}). Both the shear velocity and the critical shear velocity are unknown, but can be expressed in known parameters. The shear velocity can be expressed via:

$$u^* = u\frac{g^{0.5}}{C'} \tag{A2}$$

in which u is the time and depth-averaged velocity (m s^{-1}) derived from the measurements with the UB-LAB 2C and C' is the grain-related Chézy parameter (m$^{0.5}$ s^{-1}), which can be expressed as:

$$C' = 18log\frac{12R_h}{3D_{90}} \tag{A3}$$

Herein, R_h is the hydraulic radius, which is equal to the cross-sectional area (A) divided by the wetted perimeter (P = width + $2h$) .

The critical shear velocity can be calculated as:

$$u_c^* = \sqrt{\frac{\tau_c}{\rho_w}} \tag{A4}$$

In turn, the critical shear stress can calculated using the critical Shields number θ_c:

$$\tau_c = \theta_c(\rho_s - \rho_w)gD_{50} \tag{A5}$$

and θ_c is obtained from (Parker et al., 2003):

$$\theta_c = 0.5\left(0.22Re_p^{-0.6} + 0.06 * 10^{(-7.7Re_p^{-0.6})}\right) \tag{A6}$$

In which the particle Reynolds number, Re_p (-), is defined as:

$$Re_p = D_{50}^{3/2}\frac{\sqrt{\rho_r g}}{\nu} \tag{A7}$$

Venditti and Bradley (2022)'s empirical equation for predicting dune height and length can be found in equation (8) and (9). The dimensionless shear stress θ is derived by calculating the shear stress τ from the shear velocity (via equation (A4), replacing τ for τ_c). The critical shear stress θ_c is calculated via equation (A6).

The geometry of ripples is predicted based on Soulsby et al. (2012) via equation (10) and (11) in which D^* (-) is given by:

$$D^* = D_{50}\left(\frac{g(\frac{\rho_s}{\rho_w} - 1)}{\nu^2}\right)^{1/3} \tag{A8}$$

Appendix B Hydraulic roughness determination

For a water column that satisfies equation (12), the equation can be rewritten into:

$$\overline{u}(\sigma_d) = \frac{u^*}{\kappa}(ln(\sigma_d) + 1) + U \tag{B1}$$

in which U is the depth-mean velocity, and σ_d is the dimensionless depth using:

$$\sigma_d = \frac{z + h}{h} \tag{B2}$$

The value of u^* can be derived from the slope of a linear regression line through the data points of $\overline{u}$ versus (ln(σ_d)+1). The average velocity $\overline{u}(\sigma_d)$ was determined as the average streamwise velocity during a single measurement. The averaging time window of 30 minutes was narrowed down to cover an integer number of bedforms, defined from top to top. The σ_d-coordinate was defined such that σ_d=0 coincides with the top of the highest bedform during a measurement (the 95-percentile of the measured bed elevation was chosen, to exclude outliers as a result of backscatter spikes). The σ_d=1-coordinate is located at the top of the vertical measuring range, which corresponds to the elevation of the UB-Lab-2C transducer. The time-averaged relation between $\overline{u}$ and $ln(\sigma_d)$ was consistently linear at the middle half of the measured profile (between -0.175 $< \sigma_d <$ -0.625), so this part of the profile was used for determining u^* (Supplementary Figure S7). The goodness of the linear fit of the log-profiles had on average a R^2-value of 0.96. Following Hoitink et al. (2009), the roughness length z_0 (m) can be calculated using:

$$z_0 = \frac{h}{e^{\left(\frac{\kappa U}{u^*}\right)} + 1} \tag{B3}$$

Finally, Manning's n, n_{man} (s m$^{-1/3}$) can be calculated in the following steps (Pope, 2000; Chow, 1959):

$$k_b = 30 * z_0 \tag{B4}$$

$$n_{man} = \frac{k_b^{\frac{1}{6}}}{25} \tag{B5}$$

in which k_b is the total roughness height (m).

Roughness height can also be approximated indirectly based on the predictor of van Rijn (1984) with equation (13), resulting in the dimensionless Darcy-Weisbach friction factor, $\hat{f}$. Herein, k_s consists of form roughness height k_{sf} and grain roughness height k_{sg}:

$$k_s = k_{sg} + k_{sf} \tag{B6}$$

$$k_{sg} = 3D_{90} \tag{B7}$$

$$k_{sf} = 1.1\gamma_d\Delta(1 - e^{\frac{-25\Delta}{\lambda}}) \tag{B8}$$

where the calibration constant γ_d is taken as 1 in laboratory conditions (van Rijn, 1984).

The friction factor, $\hat{f}$, can be converted to Manning's n (n_{man}) via the Chézy coefficient C ($\mathrm{m}^{1/2}s^{-1}$) (Manning, 1891; Silberman et al., 1963).

$$C = \frac{R_h^{1/6}}{n_{man}} \tag{B9}$$

$$\hat{f} = \frac{8g}{C^2} \tag{B10}$$

Open Research Section

The data and code used to generate the results in this study will be made available through the public repository of 4TU upon acceptance, with doi: 10.4121/dde430c4-7f9f-4d7b-bff1-d4792e0031f2.

Acknowledgments

SdL and TH were funded by the Netherlands Organization for Scientific Research (NWO), within Vici project "Deltas out of shape: regime changes of sediment dynamics in tide-influenced deltas" (Grant NWO-TTW 17062). IN is funded by the Dutch Ministry of Infrastructure and Water under the research program "Rivers2Morrow". This work is based on the MSc thesis of SV and JL. We would like to thank Maarten Kleinhans and Jeremy Venditti for their help with data interpretation, Nick Wallerstein for the technical and practical help in the laboratory, and finally all fellow colleagues that helped shovelling sediment in and out of the flume.

References

Allen, J. R.L. (1978). "Computational models for dune time-lag: calculations using Stein's rule for dune height". In: *Sedimentary Geology* 20.C, pp. 165–216. ISSN: 00370738. DOI: 10.1016/0037-0738(78)90054-4.

ASCE Task Force (2002). "Flow and transport over dunes". In: *Journal of Hydraulic Engineering* 127, pp. 726–728.

Baas, J.H. and H. de Koning (1995). "Washed-Out Ripples: Their Equilibrium Dimensions, Migration Rate, and Relation to Suspended-Sediment Concentration in Very Fine Sand". In: *SEPM Journal of Sedimentary Research* Vol. 65A. ISSN: 1527-1404. DOI: 10.1306/D42680E5-2B26-11D7-8648000102C1865D.

Baas, Jaco H. (1994). "A flume study on the development and equilibrium morphology of current ripples in very fine sand". In: *Sedimentology* 41.2, pp. 185–209. ISSN: 13653091. DOI: 10.1111/j.1365-3091.1994.tb01400.x.

— (Feb. 1999). "An empirical model for the development and equilibrium morphology of current ripples in fine sand". In: *Sedimentology* 46.1, pp. 123–138. ISSN: 00370746. DOI: 10.1046/j.1365-3091.1999.00206.x.

Baas, Jaco H. and James L. Best (Aug. 2000). "Ripple formation induced by biogenic mounds—comment". In: *Marine Geology* 168.1-4, pp. 145–151. ISSN: 00253227. DOI: 10.1016/S0025-3227(00)00040-2.

Baas, Jaco H., Alan G. Davies, and Jonathan Malarkey (Jan. 2013). "Bedform development in mixed sand–mud: The contrasting role of cohesive forces in flow and bed". In: *Geomorphology* 182, pp. 19–32. ISSN: 0169555X. DOI: 10.1016/j.geomorph.2012.10.025.

Bartzke, Gerhard et al. (2013). "On the stabilizing influence of silt on sand beds". In: *Journal of Sedimentary Research* 83.8, pp. 691–703. ISSN: 15271404. DOI: 10.2110/jsr.2013.57.

Best, Jim (2005). "The fluid dynamics of river dunes: A review and some future research directions". In: *Journal of Geophysical Research: Earth Surface* 110.4, pp. 1–21. ISSN: 21699011. DOI: 10.1029/2004JF000218.

Best, Jim and John Bridge (1992). "The morphology and dynamics of low amplitude bedwaves upon upper stage plane beds and the preservation of planar laminae". In: *Sedimentology* 39.5, pp. 737–752. ISSN: 13653091. DOI: 10.1111/j.1365-3091.1992.tb02150.x.

Bradley, Ryan W. and Jeremy G. Venditti (Feb. 2017). *Reevaluating dune scaling relations.* DOI: 10.1016/j.earscirev.2016.11.004.

— (2019). "Transport Scaling of Dune Dimensions in Shallow Flows". In: *Journal of Geophysical Research: Earth Surface* 124.2, pp. 526–547. ISSN: 21699011. DOI: 10.1029/2018JF004832.

Buffington, John M., William E. Dietrich, and James W. Kirchner (Feb. 1992). "Friction angle measurements on a naturally formed gravel streambed: Implications for critical boundary shear stress". In: *Water Resources Research* 28.2, pp. 411–425. ISSN: 00431397. DOI: 10.1029/91WR02529.

Buffington, John M. and David R. Montgomery (Aug. 1997). "A systematic analysis of eight decades of incipient motion studies, with special reference to gravel-bedded rivers". In: *Water Resources Research* 33.8, pp. 1993–2029. ISSN: 00431397. DOI: 10.1029/96WR03190.

Chow, V.T. (1959). *Open-channel hydraulics.* McGraw-Hill Book Company, USA. ISBN: ISBN 0-07- 085906-X.

Czapiga, Matthew J., Astrid Blom, and Enrica Viparelli (June 2022). "Sediment Nourishments to Mitigate Channel Bed Incision in Engineered Rivers". In: *Journal of Hydraulic Engineering* 148.6. ISSN: 0733-9429. DOI: 10.1061/(ASCE)HY.1943-7900.0001977.

Dade, W. Brian and Peter F. Friend (Nov. 1998). "Grain-Size, Sediment-Transport Regime, and Channel Slope in Alluvial Rivers". In: *The Journal of Geology* 106.6, pp. 661–676. ISSN: 0022-1376. DOI: 10.1086/516052.

de Lange, S.I. et al. (2024). "Bimodality in subaqueous dune height suggests critical transition at high flow". In: *Research Square.* DOI: https://www.researchsquare.com/article/rs-3975821/latest.

de Ruijsscher, T.V. et al. (2018). "Application of a Line Laser Scanner for Bed Form Tracking in a Laboratory Flume". In: *Water Resources Research* 54.3, pp. 2078–2094. ISSN: 19447973. DOI: 10.1002/2017WR021646.

Dietrich, William E. (Dec. 1982). "Settling velocity of natural particles". In: *Water Resources Research* 18.6, pp. 1615–1626. ISSN: 00431397. DOI: 10.1029/WR018i006p01615.

Dietrich, William E. et al. (July 1989). "Sediment supply and the development of the coarse surface layer in gravel-bedded rivers". In: *Nature* 340.6230, pp. 215–217. ISSN: 0028-0836. DOI: 10.1038/340215a0.

Einstein, H. A. (1950). "The bed-load function for sediment transportation in open channel flows". In: *Technical Bulletins 156389, United States Department of Agriculture, Economic Research Service.*

Engelund, F. and E. Hansen (1967). "Monograph on Sediment Transport". In: *Technisk Forlag, Copenhagen, Denmark.*

Ferguson, R I and M Church (2004). *A simple universal equation for grain settling velocity.* Tech. rep. 6, pp. 933–937. URL: http://pubs.geoscienceworld.org/sepm/jsedres/article-pdf/74/6/933/2821499/933.pdf.

Frings, Roy M., Maarten G. Kleinhans, and Stefan Vollmer (Dec. 2008). "Discriminating between pore-filling load and bed-structure load: A new porosity-based method, exemplified for the river Rhine". In: *Sedimentology* 55.6, pp. 1571–1593. ISSN: 13653091. DOI: 10.1111/j.1365-3091.2008.00958.x.

Greene, H. Gary, Matthew Baker, and John Aschoff (2020). "A dynamic bedforms habitat for the forage fish Pacific sand lance, San Juan Islands, WA, United States". In: *Seafloor Geomorphology as Benthic Habitat.* Elsevier, pp. 267–279. DOI: 10.1016/B978-0-12-814960-7.00014-2.

Gyr, A. and A. Müller (1996). "The role of coherent structures in developing bedforms during sediment transport". In: *Coherent flow structures in open channels*, pp. 227–235.

Healy, T., Y. Wang, and J.A. Healy (2002). *Muddy Coasts of the World: Processes, Deposits and Function.* 1st ed. Amsterdam: Elsevier.

Hill, Kimberly M. et al. (Jan. 2017). "Experimental study of the effect of grain sizes in a bimodal mixture on bed slope, bed texture, and the transition to washload". In: *Water Resources Research* 53.1, pp. 923–941. ISSN: 19447973. DOI: 10.1002/2016WR019172.

Hoitink, A. J.F., F. A. Buschman, and B. Vermeulen (2009). "Continuous measurements of discharge from a horizontal acoustic Doppler current profiler in a tidal river". In: *Water Resources Research* 45.11, pp. 1–13. ISSN: 00431397. DOI: 10.1029/2009WR007791.

Hurther, D. and U. Lemmin (2001). "A Correction Method for Turbulence Measurements with a 3D Acoustic Doppler Velocity Profiler". In: *Journal of Atmospheric and Oceanic Technology*, pp. 446–458. DOI: https://doi.org/10.1175/1520-0426(2001)018<0446:ACMFTM>2.0.CO;2.

Ikeda, H. (1984). "Flume experiments on the superior mobility of sediment mixtures". In: *Ann. Rep. Inst. Geosci. 10.* Univ. of Tsukuba, Tsukuba, Japan, pp. 53–56.

Karim, F. (1995). "Bed configuration and hydraulic resistance in alluvial-channel flows". In: *Journal of Hydraulic Engineering* 121.1, pp. 15–25.

Kirchner, JAMES W. et al. (Aug. 1990). "The variability of critical shear stress, friction angle, and grain protrusion in water-worked sediments". In: *Sedimentology* 37.4, pp. 647–672. ISSN: 0037-0746. DOI: 10.1111/j.1365-3091.1990.tb00627.x.

Kwoll, E. et al. (Mar. 2016). "Flow structure and resistance over subaquaeous high- and low-angle dunes". In: *Journal of Geophysical Research: Earth Surface* 121.3, pp. 545–564. ISSN: 21699011. DOI: https://doi.org/10.1002/2015JF003637.

Lefebvre, Alice and Julia Cisneros (July 2023). "The influence of dune lee side shape on time-averaged velocities and turbulence". In: *Earth Surface Dynamics* 11.4, pp. 575–591. ISSN: 2196-632X. DOI: 10.5194/esurf-11-575-2023.

Lefebvre, Alice, Andries J. Paarlberg, and Christian Winter (Feb. 2014). "Flow separation and shear stress over angle-of-repose bed forms: A numerical investigation". In: *Water Resources Research* 50.2, pp. 986–1005. ISSN: 00431397. DOI: 10.1002/2013WR014587.

Lefebvre, Alice and Christian Winter (2016). "Predicting bed form roughness: the influence of lee side angle". In: *Geo-Marine Letters* 36.2, pp. 121–133. ISSN: 14321157. DOI: 10.1007/s00367-016-0436-8.

Li, Zhenlin and D. Komar Paul (June 1986). "Laboratory measurements of pivoting angles for applications to selective entrainment of gravel in a current". In: *Sedimentology* 33.3, pp. 413–423. ISSN: 0037-0746. DOI: 10.1111/j.1365-3091.1986.tb00545.x.

Ma, Hongbo et al. (2017). "The exceptional sediment load of fine-grained dispersal systems: Example of the Yellow River, China". In: *Science Advances* 3.5, pp. 1–8. ISSN: 23752548. DOI: 10.1126/sciadv.1603114.

Ma, Hongbo et al. (2020). "Universal relation with regime transition for sediment transport in fine-grained rivers". In: *Proceedings of the National Academy of Sciences of the United States of America* 117.1, pp. 171–176. ISSN: 10916490. DOI: 10.1073/pnas.1911225116.

Manning, R. (1891). "On the flow of water in open channels and pipes". In: *Transactions of the Institution of Civil engineers of Ireland.*

McCarron, Connor J. et al. (Apr. 2019). "The hiding-exposure effect revisited: A method to calculate the mobility of bimodal sediment mixtures". In: *Marine Geology* 410, pp. 22–31. ISSN: 00253227. DOI: 10.1016/j.margeo.2018.12.001.

Mehta, A.J. (2014). *An Introduction to Hydraulics of Fine Sediment Transport.* Ed. by N. J. Hackensack. World Scientific.

Mignot, E., D. Hurther, and E. Bartelemy (Nov. 2009). "On the structure of shear stress and turbulent kinetic energy flux across the roughness layer of a gravel-bed channel flow". In: *Journal of Fluid Mechanics* 638, pp. 423–452. ISSN: 0022-1120. DOI: 10.1017/S0022112009990772.

Naqshband, S., J.S. Ribberink, and S.J.M.H. Hulscher (2014). "Using both free surface effect and sediment transport mode parameters in defining the morphology of river dunes and their evolution to upper stage plane beds". In: *Journal of Hydraulic Engineering* 140.6, pp. 1–6. ISSN: 19437900. DOI: 10.1061/(ASCE)HY.1943-7900.0000873.

Naqshband, S. et al. (2016). "Modeling river dune development and dune transition to upper stage plane bed". In: *Earth Surface Processes and Landforms* 41.3, pp. 323–335. ISSN: 10969837. DOI: 10.1002/esp.3789.

Parker, Gary et al. (2003). "Effect of Floodwater Extraction on Mountain Stream Morphology". In: *Journal of Hydraulic Engineering* 129.11, pp. 885–895. ISSN: 0733-9429. DOI: 10.1061/(asce)0733-9429(2003)129:11(885).

Parsons, Daniel R. et al. (2016). "The role of biophysical cohesion on subaqueous bed form size". In: *Geophysical Research Letters* 43.4, pp. 1566–1573. ISSN: 19448007. DOI: 10.1002/2016GL067667.

Patel, Shaileshkumar B, Prem Lal Patel, and Prakash Devidas (2013). *Threshold for initiation of motion of unimodal and bimodal sediments.* Tech. rep. 1, pp. 24–33.

Perillo, Mauricio M., James L. Best, and Marcelo H. Garcia (2014). "A new phase diagram for combined-flow bedforms". In: *Journal of Sedimentary Research* 84.4, pp. 301–313. ISSN: 15271404. DOI: 10.2110/jsr.2014.25.

Pope, Stephen B (2000). *Turbulent Flows.* Cambridge University Press.

Prokocki, Eric W. et al. (June 2022). "The morphology of fluvial-tidal dunes: Lower Columbia River, Oregon/Washington, USA". In: *Earth Surface Processes and Landforms* 47.8, pp. 2079–2106. ISSN: 10969837. DOI: 10.1002/esp.5364.

Rouse, H. (1937). "Modern conceptions of the mechanics of turbulence". In: *Transactions American Society of Civil Engineers* 102, pp. 463–543.

Saunderson, Houston C and Francis P J Lockett (1983). "Flume experiments on bedforms and structures at the dune-plane bed transition". In: *Spec Publs. int. Ass Sediment* 6, pp. 49–58.

Schindler, Robert J. et al. (2015). "Sticky stuff: Redefining bedform prediction in modern and ancient environments". In: *Geology* 43.5, pp. 399–402. ISSN: 19432682. DOI: 10.1130/G36262.1.

SICK (2012). *Ranger E/D reference manual – MultiScan 3D camera with Gigabit Ethernet (E), 3D camera with Gigabit Ethernet (D).* Tech. rep. Waldkirch, Germany: SICK Sensor Intelligence.

Silberman, E. et al. (1963). "Friction factors in open channels". In: *J. Hydraul. Eng.* 89.HY2, pp. 97–143.

Smith, J. Dungan and S. R. McLean (Apr. 1977). "Spatially averaged flow over a wavy surface". In: *Journal of Geophysical Research* 82.12, pp. 1735–1746. ISSN: 01480227. DOI: 10.1029/JC082i012p01735.

Soulsby, R. L., R. J.S. Whitehouse, and K. V. Marten (Apr. 2012). "Prediction of time-evolving sand ripples in shelf seas". In: *Continental Shelf Research* 38, pp. 47–62. ISSN: 02784343. DOI: 10.1016/j.csr.2012.02.016.

Southard, John B and Lawrence A Boguchwal (1990). "Bed configurations in steady unidirectional water flows, part 2. Synthesis of flume data." In: 60.5, pp. 658–679.

van den Berg, J.H. and A. van Gelder (1993). "A new bedform stability diagram, with emphasis on the transiton of ripples to plane bed in flows over fine sand and silt". In: *Spec. Publs Int. Ass. Sediment* 17, pp. 11–21.

van der Mark, C. F. and A. Blom (2007). *A new and widely applicable tool for determining the geometric properties of bedforms.* Tech. rep. University of Twente.

van Rijn, L.C. (1984). "Sediment transport, part III: Bedforms". In: *Journal of Hydraulic Engineering* 110.12, pp. 1733–1754.

van Rijn, Leo C. (Jan. 2020). "Erodibility of Mud–Sand Bed Mixtures". In: *Journal of Hydraulic Engineering* 146.1. ISSN: 0733-9429. DOI: 10.1061/(asce)hy.1943-7900.0001677.

Venditti, J. G. et al. (July 2010). “Mobilization of coarse surface layers in gravel-bedded rivers by finer gravel bed load”. In: *Water Resources Research* 46.7. ISSN: 19447973. DOI: 10.1029/2009WR008329.

Venditti, Jeremy G. and Sean J. Bennett (Sept. 2000). “Spectral analysis of turbulent flow and suspended sediment transport over fixed dunes”. In: *Journal of Geophysical Research: Oceans* 105.C9, pp. 22035–22047. ISSN: 0148-0227. DOI: 10.1029/2000JC900094.

Venditti, Jeremy G. and Ryan W. Bradley (Jan. 2022). “Bedforms in Sand Bed Rivers”. In: *Treatise on Geomorphology*. Elsevier, pp. 222–254. ISBN: 9780128182352. DOI: 10.1016/B978-0-12-409548-9.12519-9.

Venditti, Jeremy G., C. Y. Martin Lin, and Moslem Kazemi (June 2016). “Variability in bedform morphology and kinematics with transport stage”. In: *Sedimentology* 63.4, pp. 1017–1040. ISSN: 13653091. DOI: 10.1111/sed.12247.

Warmink, J. J. et al. (2013). “Quantification of uncertainty in design water levels due to uncertain bed form roughness in the Dutch river Waal”. In: *Hydrological Processes* 27.11, pp. 1646–1663. ISSN: 08856087. DOI: 10.1002/hyp.9319.

Whiting, P.J. et al. (1988). “Bedload sheets in hetrogeneous sediment”. In: *Geology* 16.2, pp. 105–108. DOI: https://doi.org/10.1130/0091-7613(1988)016{\%}3C0105:BSIHS{\%}3E2.3.CO;2.

Wilcock, Peter R. (Apr. 1993). “Critical Shear Stress of Natural Sediments”. In: *Journal of Hydraulic Engineering* 119.4, pp. 491–505. ISSN: 0733-9429. DOI: 10.1061/(ASCE)0733-9429(1993)119:4(491).

Williams, Philip B. and Patrick H. Kemp (Apr. 1971). “Initiation of Ripples on Flat Sediment Beds”. In: *Journal of the Hydraulics Division* 97.4, pp. 505–522. ISSN: 0044-796X. DOI: 10.1061/JYCEAJ.0002932.

Wolanski, Eric (2007). *Estuarine Ecohydrology*. Elsevier Science. ISBN: 9780444530660. DOI: 10.1016/B978-0-444-53066-0.X5001-6.

Wu, Yongsheng et al. (2022). “Tidal propagation in the Lower Fraser River, British Columbia, Canada”. In: *Estuarine, Coastal and Shelf Science* 264.November 2021, p. 107695. ISSN: 02727714. DOI: 10.1016/j.ecss.2021.107695. URL: https://doi.org/10.1016/j.ecss.2021.107695.

Yager, Elowyn M. et al. (2018). “The trouble with shear stress”. In: *Geomorphology* 323, pp. 41–50. DOI: 10.1016/j.geomorph.2018.09.008.

Yalin, M.S. (1964). “Geometrical Properties of Sand Wave”. In: *Journal of Hydraulic Engineering* 90, pp. 105–119.

— (1972). *Mechanics of Sediment Transport*. Oxford: Pergamon Press.

Yao, Peng et al. (Sept. 2022). “Erosion Behavior of Sand-Silt Mixtures: Revisiting the Erosion Threshold”. In: *Water Resources Research* 58.9. ISSN: 19447973. DOI: 10.1029/2021WR031788.